



# Theoretical calculation guided electrocatalysts design: Nitrogen saturated porous Mo<sub>2</sub>C nanostructures for hydrogen production



Zilong Wang<sup>a,1</sup>, Heng Luo<sup>a,1</sup>, Rui Lin<sup>a,b,c</sup>, Hang Lei<sup>a,b</sup>, Yufei Yuan<sup>a,d</sup>, Zonglong Zhu<sup>d</sup>, Xibo Li<sup>a,\*</sup>, Wenjie Mai<sup>a,\*</sup>

<sup>a</sup> Siyuan Laboratory, Guangdong Provincial Engineering Technology Research Center of Vacuum Coating Technologies and New Energy Materials, Department of Physics, Jinan University, Guangzhou 510632, People's Republic of China

<sup>b</sup> Department of Chemistry, Jinan University, Guangzhou, Guangdong 510632, People's Republic of China

<sup>c</sup> School of Engineering, Westlake University, Hangzhou, Zhejiang 310024, People's Republic of China

<sup>d</sup> Department of Chemistry, City University of Hong Kong, Kowloon, Hong Kong

## ARTICLE INFO

### Keywords:

Hydrogen evolution reaction  
N-Doped molybdenum carbide  
DFT calculation  
Nickel carbide

## ABSTRACT

Herein, based on our DFT-calculation, it is the first time to uncover the fact that the catalytic property of Mo<sub>2</sub>C is related to the concentration of doped-N atoms which plays a critical role in weakening the hydrogen absorption ability of Mo<sub>2</sub>C electrocatalysts and enhancing their catalytic property. When its surface is saturated with N atoms, Mo<sub>2</sub>C exhibits the best catalytic performance. Guided by this calculation result we highlight a strategy to synthesize Mo<sub>2</sub>C electrocatalysts whose surface is fully occupied by N atoms. Our electrocatalysts exhibit a low overpotential of 57 mV vs. RHE at the current density of 10 mA cm<sup>-2</sup> and a small Tafel slope of 80 mV dec<sup>-1</sup> in 1.0 M KOH for HER which is comparable with the commercial Pt-based electrocatalyst (overpotential of 39 mV at 10 mA cm<sup>-2</sup>, Tafel slope of 69 mV dec<sup>-1</sup>). Moreover, our strategy is regarded as a general method which is successfully extended and applied to improve other metal carbide electrocatalysts such as nickel carbide. This work will pave a way for the understanding and optimization of metal carbide electrocatalysts in HER.

## 1. Introduction

Hydrogen is recognized as a promising substitute for fossil fuels. Among various methods of hydrogen production, electrocatalytic hydrogen evolution reaction (HER) by renewable energy source in alkaline media opens a green avenue for hydrogen generation. [1–3] Platinum-based electrocatalysts are the most efficient and commonly used electrocatalysts for HER because their free energy of hydrogen absorption ( $\Delta G_{H^*}$ ) is close to zero. [4,5] This suitable  $\Delta G_{H^*}$  would lead to ideal H<sub>2</sub> production on the surface of electrocatalysts and result in low overpotential for HER. Unfortunately, the scarcity and high cost of Pt greatly hamper the widespread and large-scale applications of this technology. [6] Recently, earth abundant transition metal carbides such as molybdenum (Mo) and tungsten (W) carbides have been suggested as substitutes for Pt due to their analogous electronic structures to that of Pt, wide distribution in nature and favorable catalysis property [7–10]. Specifically, dependent on intrinsic electron structure, they exhibit “platinum-like” hydrogen binding energy on catalytic centers and metallic-like transport nature [11,12]. Therefore, the molybdenum carbide

catalyst serves as a fundamental electrocatalyst in many reports with practical electrocatalyst design. Although many effects have been made, their catalytic performance in HER is still lower than that of Pt. The unsatisfactory catalytic performance is mainly due to the unsuitable bond strength of Mo-H generated from their empty d-orbitals, which limits the desorption process of adsorbed H to generate H<sub>2</sub> and results in high  $\Delta G_{H^*}$  (i.e., the Heyrovsky/Tafel step) [13–15]. Thus, it is necessary to understand the mechanism of the catalytic activity and optimize electron density for rational design of efficient Mo based catalysts with low  $\Delta G_{H^*}$  and high catalytic property. Until now, some researchers have developed some effective ways to downshift the density of empty d-band by optimizing H-binding such as facile non-metal doping, and consequently promote the HER kinetics [16–19]. However, the relationship between the nitrogen concentration and catalytic performance in HER reaction is still unclear. Moreover, controllable synthesis of metal carbides with desirable porous structures towards high catalytic property is difficult because coalescence at high carbonization temperature is inevitable [20,21]. Developing effective doped molybdenum carbides electrocatalysts and finding out the effect

\* Corresponding authors.

E-mail addresses: [lixibo@jnu.edu.cn](mailto:lixibo@jnu.edu.cn) (X. Li), [wenjiemai@email.jnu.edu.cn](mailto:wenjiemai@email.jnu.edu.cn) (W. Mai).

<sup>1</sup> These authors contribute equally to this work.

of doped N atoms in HER is necessary and will bring new ideas to the development of affordable and effective electrocatalysts for HER.

In this work, it is the first time to find out the relationship between the extent of N-doping and catalytic performance by DFT-calculation. The theoretical calculation results indicate that outstanding catalytic performance relies on the high N concentration on the surface of Mo<sub>2</sub>C which will contribute to weaken the hydrogen absorption ability and bring more active sites, resulting in higher catalytic properties. Based on these results, we developed a novel strategy to synthesize 3D porous N-doped Mo<sub>2</sub>C/C composite whose surface is saturated with N atoms (denoted as 3D-N-Mo<sub>2</sub>C/C) as efficient electrocatalysts for HER. The as-synthesized electrocatalysts show the following advantages: (i) The doped N atoms can reduce the  $\Delta G_{H^*}$  and generate more exposed active sites to facilitate HER. High N concentration will contribute to bring more active sites. (ii) Based on the theoretical calculation and experiment results we find that when the surface of Mo<sub>2</sub>C is saturated with N atoms, Mo<sub>2</sub>C exhibits the best catalytic performance. (iii) The porous structure and interaction between Mo<sub>2</sub>C and carbon in 3D-N-Mo<sub>2</sub>C/C can enhance the conductivity and accelerate the electron transfer in HER. Experimental investigation validates the 3D-N-Mo<sub>2</sub>C/C electrocatalysts' Pt-like catalytic property of low onset potential and small Tafel slope toward HER. This as-prepared 3D-N-Mo<sub>2</sub>C/C exhibit noteworthy electrocatalytic performance for HER in alkaline media (overpotential of 57 mV to reach the current density of 10 mA cm<sup>-2</sup>, Tafel slope of 80 mV dec<sup>-1</sup>) with excellent stability. Moreover, our strategy is applicable to developing other 3D porous nitrogen doped metal carbide such as 3D-N-Ni<sub>3</sub>C/C which presents similar catalytic performance.

## 2. Results and discussion

Based on prior study, Mo<sub>2</sub>C (JSPS, 35-0787) is an attractive electrocatalysts for HER. To understand the intrinsic between structural composition and the catalytic properties of Mo<sub>2</sub>C, first-principles calculations are carried out to explore the free energies adsorption energy ( $\Delta G_{H^*}$ ) of hydrogen on Mo<sub>2</sub>C (001) with different N doping concentrations. In this work, a six-atomic-layers of (4 × 4) (001) slab of Mo<sub>2</sub>C are established for further DFT calculations. First, the  $\Delta G_{H^*}$  on perfect Mo<sub>2</sub>C (001) are explored. There are three possible adsorption sites for hydrogen on perfect Mo<sub>2</sub>C (001) (denoted by Mo<sub>2</sub>C(001)@): C-T (Top), H-1 (HCP), and F-1 (FCC), as in shown in Fig. 1a. The  $\Delta G_{H^*}$  on the three active sites are -0.57, -0.18 and -0.13 eV, respectively, and close to the previous DFT calculations [22]. Obviously, the values of  $|\Delta G_{H^*}|$  on H-1 and F-1 are much smaller than that on C-T op, indicating H-1 and F-1 are active sites during the HER electrocatalytic process and show higher HER activity. The different adsorption ability among these three sites is strongly related to the number of the broken bonds of the C and Mo atoms in the top layer of the surface. The C atoms in the top layer of Mo<sub>2</sub>C(001)@ have three bonds less when compared with those in the bulk whereas the Mo atoms in the top layer have the same number. The more leaving dangling bonds for C will make H adsorption on C-T much stronger than that on H-1 and F-1.

Further DFT calculations are also carried out to explore the N doping effect on the HER activity on perfect Mo<sub>2</sub>C. When one N atom substitutes a C atom in the top layer (as shown in Fig. 1b, denoted by Mo<sub>2</sub>C(001)@1 N), the adsorption ability of H around the N atom will become weaker: the  $\Delta G_{H^*}$  on N-T, F-2 site will be -0.21 and -0.10 eV, respectively, about 0.36 and 0.03 eV higher than that on the corresponding sites on Mo<sub>2</sub>C(001)@. The much weaker adsorption ability of H indicates the higher HER activity once one N substitute the C atom in Mo<sub>2</sub>C. Meanwhile, the  $\Delta G_{H^*}$  on H-1 and C-T -2 site on Mo<sub>2</sub>C(001)@1 N is -0.18 and -0.57 eV, respectively, the same value as that on H-1 and C-T on Mo<sub>2</sub>C(001)@. These results clearly show the doped N atom can't modify the HER activity while the adsorption site is far from N atom, indicating the number of the active sites remained nearly unchanged. This indicates the enhancement of HER activity at lower N concentration is not remarkable. Thus, the effect of higher N doping

concentration in Mo<sub>2</sub>C(001) is also explored. The Mo<sub>2</sub>C(001)@ with half and all of the C in top layer substituted by N, are shown in Fig. 1c (Mo<sub>2</sub>C(001)@4 N) and 1d (Mo<sub>2</sub>C(001)@8 N), respectively. The  $\Delta G_{H^*}$  on F-1, F-2, N-T, C-T, H-1 and H-2 of Mo<sub>2</sub>C(001)@4 N is -0.07, -0.08, -0.10, -0.53, -0.21 and -0.20 eV, respectively. The  $|\Delta G_{H^*}|$  on the first three sites on Mo<sub>2</sub>C (001)@4 N is about 0.06, 0.05, and 0.03 eV smaller the smallest  $|\Delta G_{H^*}|$  on Mo<sub>2</sub>C(001). These three kinds of sites with decreased  $|\Delta G_{H^*}|$  on Mo<sub>2</sub>C(001)@4 N indicate more active sites, much higher HER activity, which induce much lower overpotential and larger current in N doped Mo<sub>2</sub>C in experiment part. When all of the C in the top layer of Mo<sub>2</sub>C(001)@ are substituted by N atoms, the most active situation will show even smaller  $|\Delta G_{H^*}|$ . The  $\Delta G_{H^*}$  on N-T, F-1 and H-1 of Mo<sub>2</sub>C(001)@8 N is 0.04, 0.19 and -0.26 eV, respectively. Although the number of active sites on Mo<sub>2</sub>C(001)@8 N is just comparable with that on Mo<sub>2</sub>C(001)@, the much lower  $|\Delta G_{H^*}|$  (0.04 eV) on N-T implies the N-T sites will have much higher HER activity. In summary, the relatively higher N doping concentrations in Mo<sub>2</sub>C(001)@ will show lower  $|\Delta G_{H^*}|$  and more active sites, and increase the HER activity in the end.

The free energy change of adsorbed H at a given site,  $\Delta G_{H^*}$ , is strongly related to the electronic properties of the top layer of Mo<sub>2</sub>C(001). Then we further inquire into the relationship between the  $\Delta G_{H^*}$  and band center of the corresponding atoms in the top layer for different H adsorption sites on Mo<sub>2</sub>C(001)@ and N doped Mo<sub>2</sub>C(001)@: the  $\Delta G_{H^*}$  on FCC site as a function of the d-band center of Mo atoms ( $E_d$ ) in the top layer is shown in Fig. 1i, and the  $\Delta G_{H^*}$  on the top site as a function of the p-band center of C or N atoms in the top layer ( $E_p$ ) is shown in Fig. 1j. It clearly shows that with the increase of the N doping concentration, e.g., from Mo<sub>2</sub>C(001)@ to Mo<sub>2</sub>C(001)@8 N, both  $E_d$  and  $E_p$  will be more negative, dropping further below the Fermi level. The more negative  $E_d$  and  $E_p$  will make interactions between H of FCC site and Mo atom, H of top site and C atom or N atom, much weaker. The calculated results are in accordance with the d-band model [23–25], which clearly shows the  $\Delta G_{H^*}$  has a nearly negative linear relationship with d-band center or p-band center, as shown in Fig. 1i and j, respectively. Thus, suitable N doping concentrations in Mo<sub>2</sub>C (001) will make the  $\Delta G_{H^*}$  much closer to 0 eV at a given adsorption site, e.g., the FCC site (F-2) of Mo<sub>2</sub>C(001)@4 N, the top site of N (N-T) of Mo<sub>2</sub>C(001)@8 N. In summary, the N doping in Mo<sub>2</sub>C(001) surface will tune the d-band center of Mo atoms and p-band center of C or N atoms in the top layer, therefore in turn modify the interaction between the adsorbed H and the surface of Mo<sub>2</sub>C,  $\Delta G_{H^*}$ . Moreover, the catalytic property of N-doped Mo<sub>2</sub>C is related to the N concentration on the surface. Higher content of N atoms in Mo<sub>2</sub>C can bring more active sites for HER. Guided by above DFT-calculation results, we can design suitable N doped Mo<sub>2</sub>C catalysts with maximized catalytic property. Moreover, it is the first time to uncover the relationship between the nitrogen concentration and the catalytic property of Mo<sub>2</sub>C in HER.

Fig. 2 illustrates the synthesis route of 3D-N-Mo<sub>2</sub>C/C. Typically, silica nanospheres with diameter of ~300 nm were chosen as a template to construct 3D porous structure and their scanning electron microscopy (SEM) images are shown in Fig. S1a–c. Their inner space was impregnated by molybdenum precursors. After that the collected products were heated in N<sub>2</sub> to form molybdenum carbide and subsequently etched by hydrofluoric acid to remove the template. The as-prepared sample was denoted as 3D-Mo<sub>2</sub>C/C. This 3D-Mo<sub>2</sub>C/C was then annealed in NH<sub>3</sub> to form the nitrogen doped sample (denoted as 3D-N-Mo<sub>2</sub>C/C). Moreover, to analyze the effect of N-doping, we synthesized samples with different N content by adjusting the nitriding time and temperature. All the details are shown in the Appendix A. Supplementary data.

SEM images in Fig. 3a and b reveal the as-prepared 3D-N-Mo<sub>2</sub>C/C architecture with uniform spherical vacancy derived from nanospheres template. Arranged mesoporous structures are generated after pyrolysis and nitrogen-doped process. Transmission electron microscopy (TEM) images in Fig. 3c–e further disclose that the mesoporous structure of 3D-N-Mo<sub>2</sub>C/C consists of many N-Mo<sub>2</sub>C nanoparticles which are

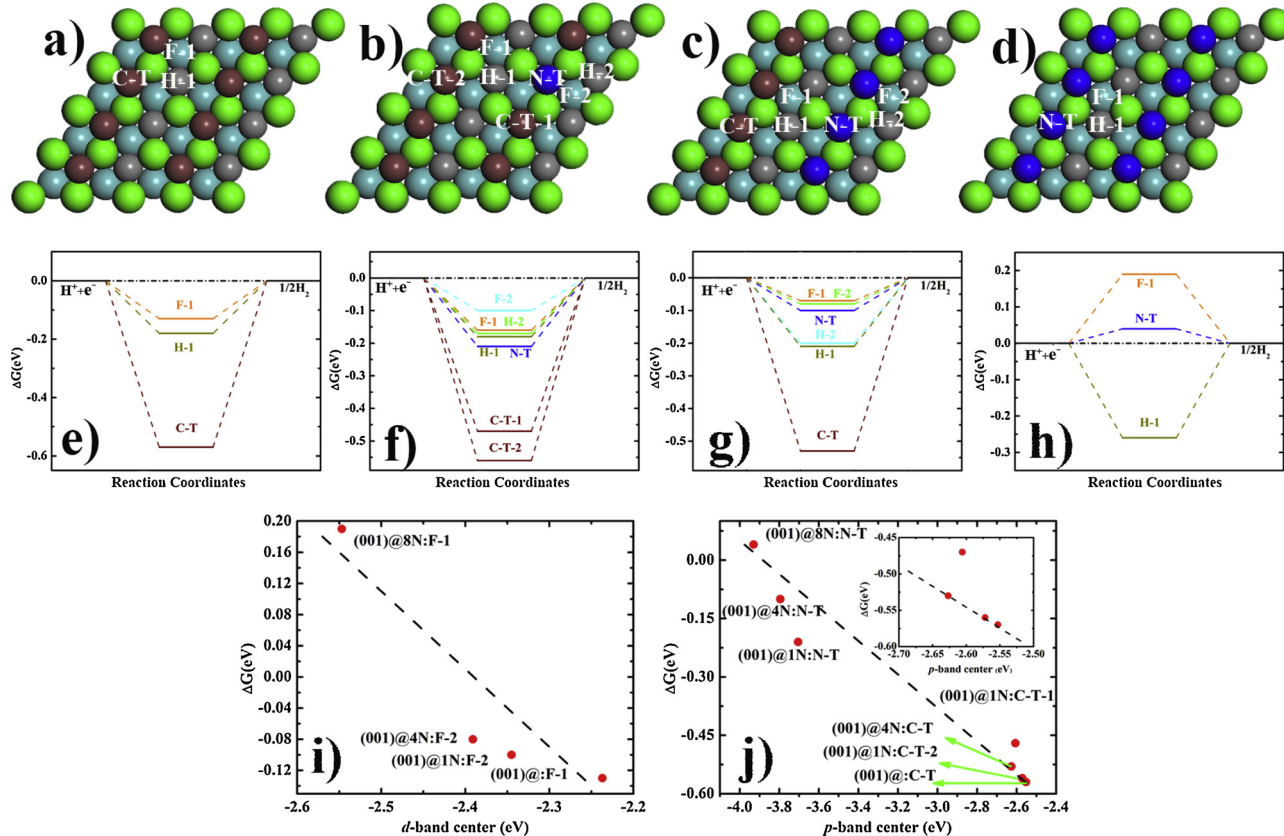


**Fig. 1.** Possible adsorption site of H on (a) Mo<sub>2</sub>C(001)@0, (b) Mo<sub>2</sub>C(001)@1 N, (c) Mo<sub>2</sub>C(001)@4 N and (d) Mo<sub>2</sub>C(001)@8 N. The middle panels of (e–h) are  $\Delta G_{H^*}$  on the corresponding structures shown in (a–d), respectively. The “F” “H” and “T” indicate the FCC, HCP and top site respectively, and “C” and “N” denote carbon and nitrogen atom respectively, e.g., “C-T-2” represents second kind adsorption site on top of carbon atom as in (b). The  $\Delta G_{H^*}$  on (i) FCC site as function of *d*-band center of Mo atoms in top layer, and (j) top site of C or N atom as function of the *p*-band center of top C or N atoms in top layer of Mo<sub>2</sub>C(001)@0, Mo<sub>2</sub>C(001)@1 N, Mo<sub>2</sub>C(001)@4 N and Mo<sub>2</sub>C(001)@8 N, respectively. The bottom right part of (j) is zoomed in and shown in inset. The corresponding H adsorption sites in (i) and (j) are as shown in (a)–(d). The turquoise, grey, green, brown, blue balls indicate the Mo atoms in the sub-layers, C atoms in the sub-layers, Mo atoms in the second top layer, C atoms in the top layer, N atoms in the top layer, respectively (For interpretation of the references to colour in this figure legend, the reader is referred to the web version of this article).

uniformly embedded in amorphous carbon matrix with a thickness of less than 5 nm. Previous studies have shown that this amorphous carbon matrix would play an important role in prohibiting the

aggregation of Mo<sub>2</sub>C nanoparticles and stabilizing them [8]. The presence of amorphous carbon is confirmed by the Raman spectrum in Fig. S2. This mesoporous structure of our sample is also confirmed by a high

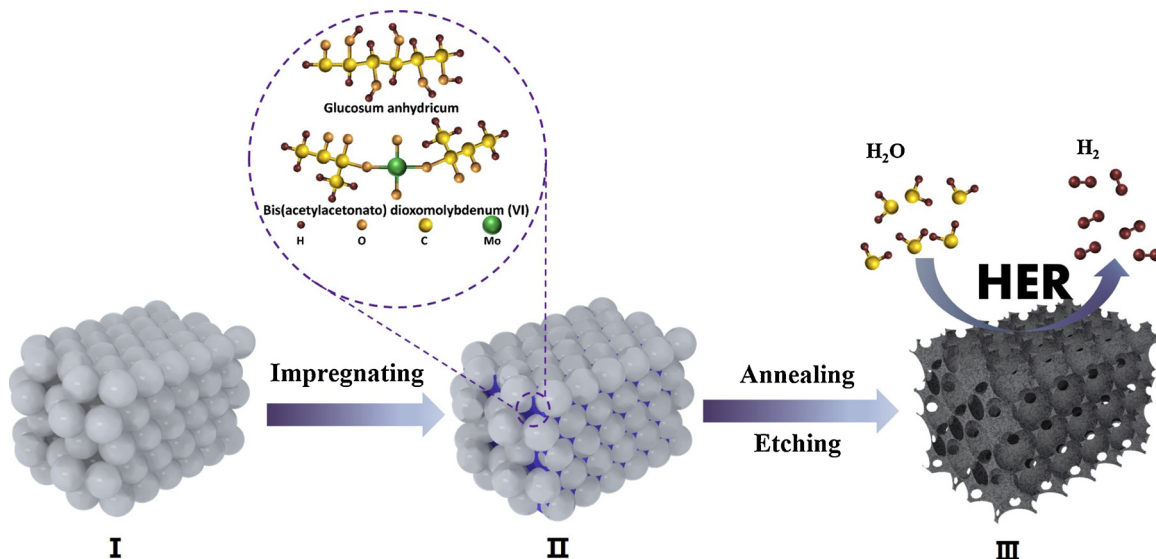


**Fig. 2.** Illustration of the formation process of the samples. I: SiO<sub>2</sub> nanospheres template. II: SiO<sub>2</sub> nanospheres template with molybdenum precursors. III: 3D-Mo<sub>2</sub>C/C and 3D-N-Mo<sub>2</sub>C/C.

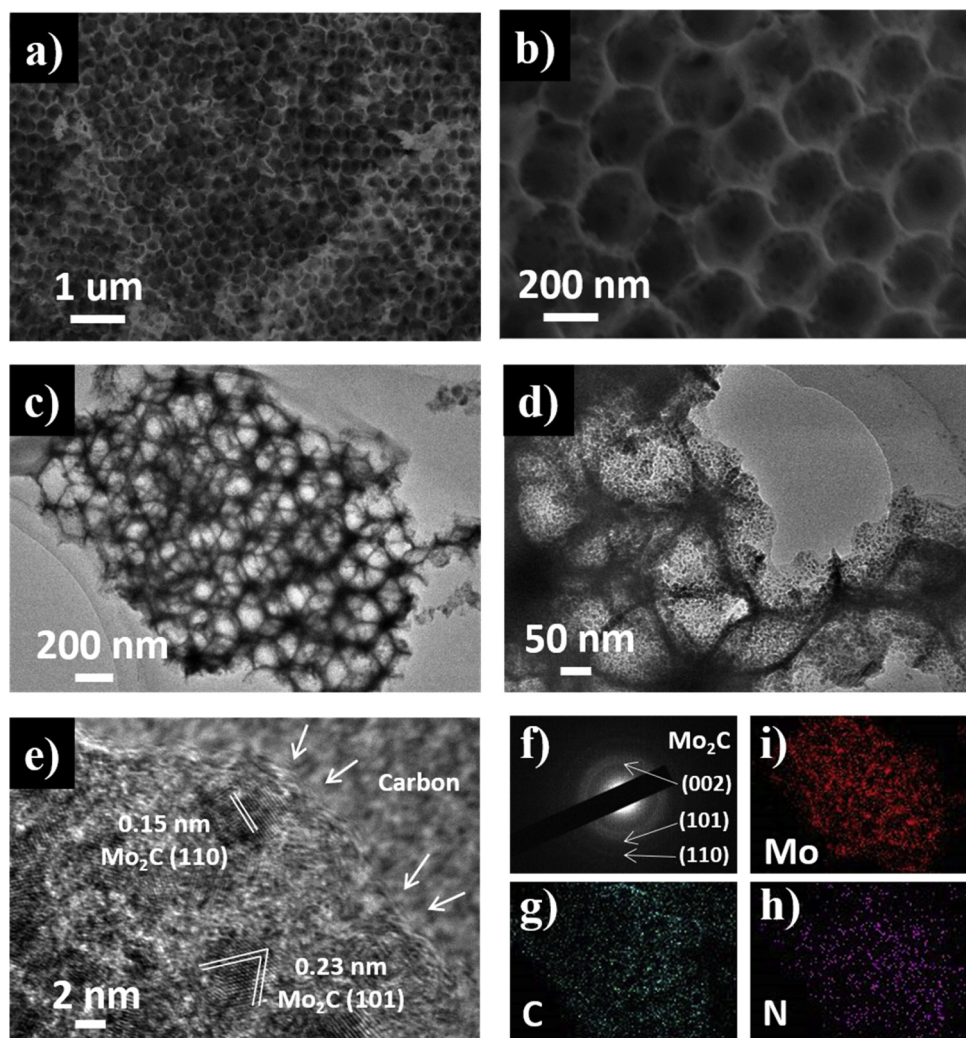


**Fig. 3.** (a) Low-magnification and (b) high-magnification SEM images of 3D-N-Mo<sub>2</sub>C/C porous catalyst. (c) and (d) TEM images of 3D-N-Mo<sub>2</sub>C/C porous catalyst. (e) HRTEM image of 3D-N-Mo<sub>2</sub>C/C. (f)-(h) SAED pattern of the 3D-N-Mo<sub>2</sub>C/C and the corresponding elemental mappings showing the distribution of C, N and Mo elements, respectively.

specific Brunauer-Emmett-Teller (BET) surface area of 479.15 m<sup>2</sup> g<sup>-1</sup>, which is much higher than other reports (Fig. S3), and abundant mesopores with average size of 4.03 nm (Fig. S4). High-resolution TEM (HRTEM) image in Fig. 3e reveals that our 3D-N-Mo<sub>2</sub>C/C has interplanar spacings of 0.15 and 0.23 nm, which are identical with those of hexagonal Mo<sub>2</sub>C (110) and (101) facets, respectively. Fig. 3f exhibits the selected-area electron diffraction (SAED) pattern of 3D-N-Mo<sub>2</sub>C/C, in which some of the characteristic diffraction rings standing for hexagonal Mo<sub>2</sub>C (002), (101) and (110) facets can be clearly observed. In order to identify the composition of 3D-N-Mo<sub>2</sub>C/C, energy dispersive X-ray (EDX) elemental mappings were obtained. These results shown in Fig. 3g-i demonstrate the homogeneous distribution of Mo, C and N atoms, respectively.

X-ray diffraction (XRD) patterns of 3D-N-Mo<sub>2</sub>C/C and 3D-Mo<sub>2</sub>C/C are exhibited in Fig. 4a and match well with hexagonal Mo<sub>2</sub>C (JCPDS No. 35-0787). Specially, no distinct new peak appears after N doping, indicating that no nitride forms. The XRD peaks of N doped sample slightly shift to a high angle direction compared to that of pure 3D-Mo<sub>2</sub>C/C (inset of Fig. 4a), illustrating a decreased lattice parameter after N doping. This phenomenon is probably caused by the replacement of some C atoms with smaller N atoms in lattice bringing the shrink in lattice parameter [22]. The above XRD results are well coincident with TEM and SAED results, indicating successful N doping in 3D-N-Mo<sub>2</sub>C/C. Raman spectrum is also collected to analyze the effect of

N doping on the carbon phase in our materials (Fig. S2). The intensity ratio of D and G bands ( $I_D/I_G$ ) locating at 1350 and 1620 cm<sup>-1</sup> can be used to evaluate the graphitized degree of carbon materials. After N doping, the  $I_D/I_G$  of 3D-N-Mo<sub>2</sub>C/C ( $I_D/I_G$  of 1.26) is higher than that of pure one (3D-Mo<sub>2</sub>C/C,  $I_D/I_G$  of 1.18). This slight increase indicates a relatively lower graphitized degree which conduces to introduce more active sites and ion transport tunnels [26,27]. The higher  $I_D/I_G$  of 3D-N-Mo<sub>2</sub>C/C mainly comes from the doped N atoms which increase the content of defects in graphitized carbon [28]. X-ray photoelectron spectroscopy (XPS) and ultraviolet photoelectron spectroscopy (UPS) results are collected to investigate the surface chemical nature of Mo, C and N elements. Fig. 4b and S6 display the peaks of Mo 3d in our samples. The peaks at 232.6, 229.7 and 228.6 eV stand for Mo 3d<sub>5/2</sub> of Mo<sup>6+</sup>, Mo<sup>4+</sup> and Mo<sup>2+</sup>, while the peaks at 235.7, 233.4 and 231.6 eV correspond to Mo 3d<sub>3/2</sub> of Mo<sup>6+</sup>, Mo<sup>4+</sup> and Mo<sup>2+</sup>, respectively [29]. The signals of Mo<sup>4+</sup> and Mo<sup>6+</sup> which indicate the presence of superficial oxides are thought to be caused by the oxidation in air [30]. In addition, the peak of Mo<sup>2+</sup> presents a red-shift of ~0.3 eV in 3D-N-Mo<sub>2</sub>C/C compared to that in 3D-Mo<sub>2</sub>C/C and the extent of offsets vary further with the change of nitrogen doping time and temperature, suggesting that N-doping provides enriched electrons around Mo [31,32]. This red-shift may come from the decrease of Mo valence state due to the partial replace of C sites by N and indicates successful N doping [16]. According to the XPS result, our nitrogen doping strategy

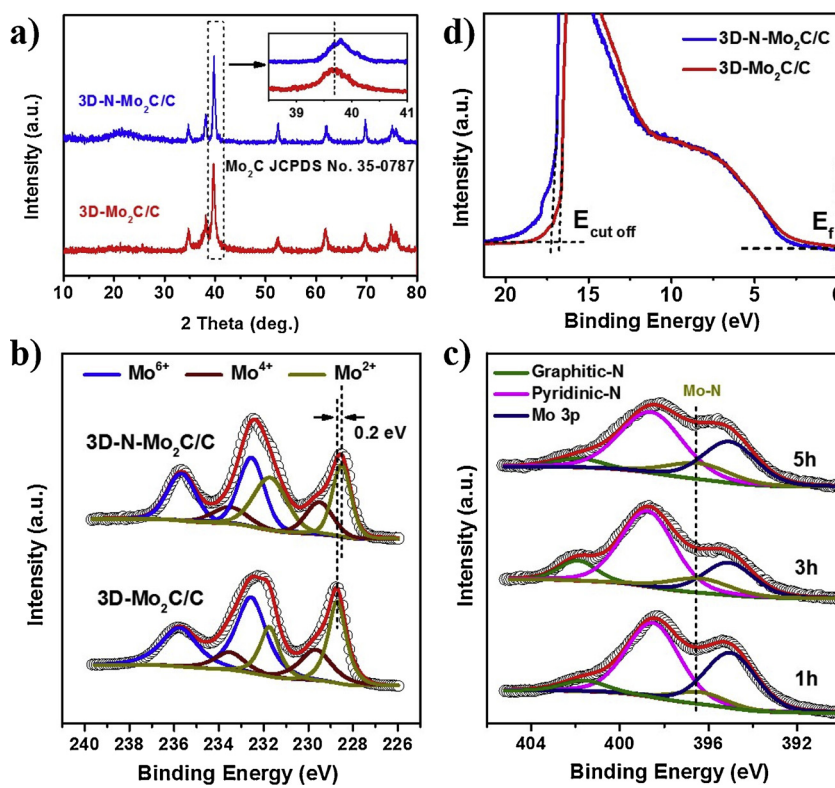


**Fig. 4.** (a) XRD patterns of 3D-Mo<sub>2</sub>C/C and 3D-N-Mo<sub>2</sub>C/C (inset: zoomed in view of XRD patterns). (b) High-resolution XPS spectra of Mo 3d spectrum of 3D-Mo<sub>2</sub>C/C and 3D-N-Mo<sub>2</sub>C/C. (c) High-resolution XPS spectra of N 1s and Mo 3p<sub>5/2</sub> spectrum of 3D-N-Mo<sub>2</sub>C/C with different nitrogen doping time at 350 °C. (d) UPS analysis of 3D-Mo<sub>2</sub>C/C and 3D-N-Mo<sub>2</sub>C/C.

can increase the percentage of Mo<sup>2+</sup> greatly on the surface of electrocatalysts (42.9% of 3D-N-Mo<sub>2</sub>C/C and 31.2% of 3D-Mo<sub>2</sub>C/C) which is regarded as the active sites for HER [33–35]. The high-resolution N 1s spectra in Fig. 4c (atomic ratio of 11.62%) of the 3D-N-Mo<sub>2</sub>C/C sample exhibits two peaks standing for pyridinic-N (398.7 eV) and graphitic-N (401.7 eV) [36]. The pyridinic and graphitic N atoms mainly come from the nitrogen-doped carbon shell which can be found in the TEM images and EDS results (Fig. 3e and h). In 3D-N-Mo<sub>2</sub>C/C, pyridinic-N is characterized by a relatively strong peak. As pyridinic-N modifies the band density of carbon, it can help to increase the  $\pi$  state to the Fermi level, thus reducing the work function and enhancing the catalytic performance of water splitting [37]. The peak position of 396.4 eV can be assigned to the Mo–N bonds [31]. It can further confirm that some N atoms have succeeded in replacing some C atoms in 3D-N-Mo<sub>2</sub>C/C. At the same time, this result is consistent with that of Mo 3d spectrum. The content of Mo–N bond in samples obtained at different nitriding temperature were summarized in Fig. 4c and S7. The sample obtained at 350 °C exhibits the highest content of Mo–N bonds. This result proves that this temperature is favourable for N doping. At this temperature we also adjusted the reaction time. As shown in Fig. 4c, the percentage of Mo–N band increases from 11.35% to 13.1% when the reaction time increases from 1 h to 3 h. However, when the nitriding time is increased to 5 h, the change in Mo–N band content is negligible (13.5%). This phenomenon proves that the N doping occurs on the surface of Mo<sub>2</sub>C and reaches saturated when the nitriding time is longer than 3 h. N atom ratio and Mo–N bond proportion of 3D-N-Mo<sub>2</sub>C at different nitrogen doping conditions are shown in Table S2 and S3. Above results indicate the successful N-doping in Mo<sub>2</sub>C and the formation of nitrogen-doped carbon shell which may render enhanced electroactivity to the materials [38]. According to the formula ( $\Phi = h\nu - (E_{\text{Cut off}} - E_{\text{Fermi}})$ ), we can calculate the work function ( $\Phi$ ) of 3D-N-Mo<sub>2</sub>C/C (3.95 eV) and 3D-Mo<sub>2</sub>C/C (4.47 eV) from the UPS results (Fig. 4d). Based on the XPS and UPS results, we find that N-doping brings enriched electron density which may benefit the HER performance. This result indicates the nitrogen doping strategy can bring smaller work function which is thought to offer a lower energetic barrier and enhance the ability to

capture electrons and optimize the catalysis performance in HER [39,40].

The HER electrocatalytic activities of 3D-N-Mo<sub>2</sub>C/C, 3D-Mo<sub>2</sub>C/C, Pt metal (pure polycrystalline), commercial 20 wt% Pt/C and bare Ni foam were evaluated in 1.0 M KOH. The loading mass of the above samples is the same to evaluate the catalytic performance. The linear sweep voltammetry (LSV) curves of 3D-N-Mo<sub>2</sub>C/C with different nitriding time and temperature of N-doping are shown in Fig. S8. We can find that the samples with saturated N atoms on the surface of Mo<sub>2</sub>C exhibit the highest electrocatalytic performance. The most superior performance of the samples with saturated N atoms on the surface of Mo<sub>2</sub>C can be attributed to the highest electrochemical active surface area (ECSA), as shown in Fig. S9. For the LSV curves shown in Fig. 5a, the HER onset potential is calculated via the intersection of the extrapolated baseline current and the prolonged tangent of the LSV characteristic curves and the onset potential of our 3D-N-Mo<sub>2</sub>C/C is only 17 mV vs. RHE, which is much lower than those of 3D-Mo<sub>2</sub>C/C (70 mV), Pt metal (63 mV) and Ni foam (145 mV). Meanwhile, it is worth noting that the onset potential of 3D-N-Mo<sub>2</sub>C/C is close to that of 20 wt% Pt/C electrocatalyst. Moreover, the 3D-N-Mo<sub>2</sub>C/C provides much lower overpotential of only 57 mV than 3D-Mo<sub>2</sub>C/C (111 mV) at the same current density of 10 mA cm<sup>-2</sup>, indicating N-doping strategy brings improved catalytic property. These results demonstrate that our 3D-N-Mo<sub>2</sub>C/C owns excellent electrocatalytic property for HER in alkaline media which is superior or comparable to most previously reported molybdenum based electrocatalysts, such as  $\beta$ -Mo<sub>2</sub>C nanotubes (112 mV for 10 mA cm<sup>-2</sup>) [41], 2D N, Co-Mo<sub>2</sub>C (92 mV for 10 mA cm<sup>-2</sup>) [29], MoC-Mo<sub>2</sub>C hetero nanowires (120 mV for 10 mA cm<sup>-2</sup>) [42], Mo<sub>2</sub>C nanoparticles (100 mV for 10 mA cm<sup>-2</sup>) [20] and others (Table S1).

As shown in Fig. 5b, the Tafel slope of 3D-N-Mo<sub>2</sub>C/C in the overpotential interval between 0.048–0.091 V is 80 mV dec<sup>-1</sup>, which is significantly smaller than those of 3D-Mo<sub>2</sub>C/C (113 mV dec<sup>-1</sup>), Pt metal (133 mV dec<sup>-1</sup>) and close to that of 20 wt% Pt/C (69 mV dec<sup>-1</sup>). This result indicates that compared with 3D-Mo<sub>2</sub>C/C the kinetic radical step of HER on 3D-N-Mo<sub>2</sub>C/C at low potential is not sluggish and the rate-determining step of our 3D-N-Mo<sub>2</sub>C/C is the H-desorption process.

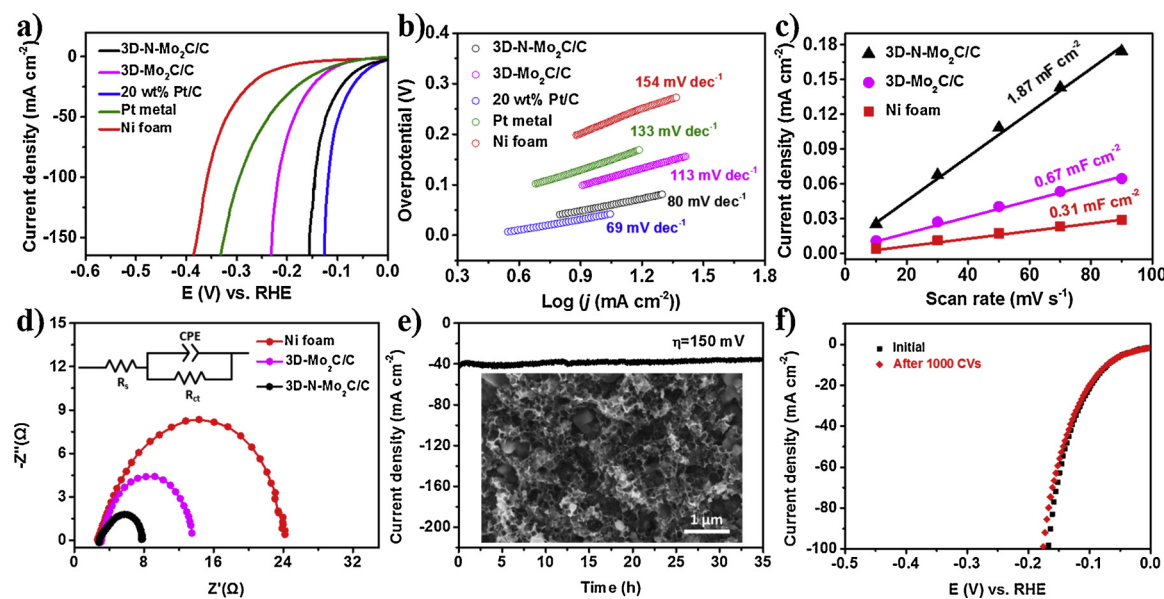


**Fig. 5.** (a) Linear sweep voltammetry (LSV) curves, (b) Tafel plots for 3D-Mo<sub>2</sub>C/C, 3D-N-Mo<sub>2</sub>C/C, Pt metal and commercial 20 wt% Pt/C coated on the Ni foam electrocatalysts in 1.0 M KOH solution at scan rate of 5 mV s<sup>-1</sup>. (c) Estimation of C<sub>dl</sub> by plotting the current density variation ( $\Delta j = (j_a - j_c)/2$ ) obtained from the CV and (d) Nyquist plots of bare Ni foam, 3D-Mo<sub>2</sub>C/C and 3D-N-Mo<sub>2</sub>C/C coated on the Ni foam electrocatalysts at 200 mV vs. RHE. The semicircle represents the charge-transfer resistance (R<sub>ct</sub>). (e) Chronoamperometry measurements of long-term stability of 3D-N-Mo<sub>2</sub>C/C for 35 h (inset: SEM images of the catalyst after durability test). (f) Polarization curves of 3D-N-Mo<sub>2</sub>C/C electrocatalyst before and after 1000 cyclic voltammetry cycles.

Based on the Tafel plots, we calculated exchange current density ( $j_0$ ) of these samples to evaluate their inherent HER property. Our 3D-N-Mo<sub>2</sub>C/C achieves a high  $j_0$  of 1.972 mA cm<sup>-2</sup> which is comparable to that of 20 wt% Pt/C (2.868 mA cm<sup>-2</sup>). Thus, the 3D-N-Mo<sub>2</sub>C/C exhibits much improved kinetic radical step for HER. In addition, as shown in Fig. S10, we also collected the performance of N-Mo<sub>2</sub>C/C without 3D structure (denoted as bulk N-Mo<sub>2</sub>C/C) in HER. In sharp contrast, 3D-N-Mo<sub>2</sub>C/C exhibits a remarkably optimized HER performance, which is about 40 mV less than that of bulk N-Mo<sub>2</sub>C/C at the current density of 10 mA cm<sup>-2</sup>. As we expected, the Tafel slope of the 3D-N-Mo<sub>2</sub>C/C is about 43 mV dec<sup>-1</sup> lower than that of bulk N-Mo<sub>2</sub>C/C. These results show that the 3D structure we designed can bring high specific surface area and promote the HER process.

Furthermore, we analyzed the effect of nitrogen doping on pure porous carbon materials. We did not add molybdenum source to the precursor in the preparation process, and synthesized three-dimensional porous carbon catalyst and nitrogen doping one (denoted as 3D-Porous-C and 3D-N Porous C). (See the Supplementary Material for details). As shown in Fig. S11, nitrogen doping improves the performance of 3D-Porous-C to a certain extent, even if the effect of improvement is low, and the overall activity is poor. This again implies that doped nitrogen atoms are conducive to enhancing the activity of carbides, and the main contribution of the large increase in activity is due to Mo-N bond. The calculation results shown in Fig. S20 exhibit similar results. In order to elucidate the minor effect of 3D-N-porous C on the HER activity, the adsorption ability of H on two kinds of N doped graphene, graphitic-N and pyridinic-N graphene, are also calculated. It clearly shows both the graphitic-N and pyridinic-N graphene will show higher HER activity than perfect graphene, which could be concluded by the smaller  $|\Delta G_{H^*}|$  for N-doped graphene. For example, the smallest  $|\Delta G_{H^*}|$  could reach 0.74 eV and 0.85 eV on graphitic-N and pyridinic-N graphene, respectively, which is much smaller than that (1.56 eV) of perfect graphene. However, the corresponding values are still much larger than that of Mo<sub>2</sub>C or N doped Mo<sub>2</sub>C, as their  $|\Delta G_{H^*}|$  could reach values smaller than 0.20 eV as discussed. Those results indicate the Mo<sub>2</sub>C and N-doped Mo<sub>2</sub>C dominate the HER activity in our research, and the contribution of N-doped carbon to HER could be ignored. At the same time, we also analyzed the properties of 3D-N-Mo<sub>2</sub>C/C with

different nitrogen doping content in HER. Polarization curves in Fig. S8c and d reveal that catalytic performance is gradually optimized with the increase of nitrogen doping concentration. When nitrogen atoms are saturated on the doped surface, 3D-N-Mo<sub>2</sub>C/C performance is slightly improved, showing the best activity. The above results are closely consistent with the theoretical calculation.

To analyze the origin of improved excellent electrocatalytic property brought by our novel strategy, we analyzed the electrochemical active surface area (ECSA) and charge transfer mechanism of these samples. The correlation between HER catalytic performance and ECSA is studied through electrochemical double-layer capacitances (C<sub>dl</sub>). As shown in Fig. 5c and S12, the C<sub>dl</sub> of 3D-N-Mo<sub>2</sub>C/C (1.87 mF cm<sup>-2</sup>) is three times larger than that of 3D-Mo<sub>2</sub>C/C (0.67 mF cm<sup>-2</sup>). This result implies that doped N atoms bring higher ECSA and results in more active sites for HER. Moreover, after corrected by ECSA, 3D-N-Mo<sub>2</sub>C/C also exhibits the most superior performance in HER (Fig. S13). Above results correspond to the calculation results. In addition, Nyquist plots in Fig. 5d indicate that the 3D-N-Mo<sub>2</sub>C/C exhibits much smaller resistance (5.29 Ω) compared with that of 3D-Mo<sub>2</sub>C/C (10.71 Ω). This result indicates our strategy can also provide a faster electron transfer rate in HER process. Furthermore, 3D-N-Mo<sub>2</sub>C/C shows much higher C<sub>dl</sub> and lower resistance, compared with bulk N-Mo<sub>2</sub>C/C in Fig. S14. The above results show that the three-dimensional porous structure can provide more active sites, and conduct to reduce the transmission impedance and increase the charge transfer rate [43–45]. Stability of electrocatalysts is also important. The chronoamperometric curve of our sample is collected at a high overpotential of 150 mV for 35 h. As shown in Fig. 5e, the current density of 3D-N-Mo<sub>2</sub>C/C exhibits negligible decrease during the entire testing period. This result suggests the 3D-N-Mo<sub>2</sub>C/C owns excellent long-term stability in HER. Moreover, after continuous reaction for 35 h, the structure and morphology of 3D-N-Mo<sub>2</sub>C/C remained intact (inset in Fig. 5e), further indicating its excellent stability. Meanwhile, as shown in Fig. 5f, the polarization curve shows a negligible change after continuously 1000 cycles of cyclic voltammetry. Fig. S15 illustrates the hydrogen and oxygen production rate of our electrocatalyst. When the current density is 5 mA cm<sup>-2</sup>, the volume ratio of H<sub>2</sub>/O<sub>2</sub> yield matches well with the value of 2:1, indicating a nearly 100% Faradaic efficiency.

The calculations and discussions above uncover the mechanism of how N doping modifies the surrounding chemical condition, changes the d-band or p-band center, tunes  $\Delta G_{\text{H}^*}$  and enhances the HER activity on Mo<sub>2</sub>C in the end. To demonstrate the universality of our strategy, 3D-N-Ni<sub>3</sub>C/C is also designed as electrocatalysts for HER. Figs. S16 and S17 show the morphology and structure of 3D-N-Ni<sub>3</sub>C/C which are similar to those of 3D-N-Mo<sub>2</sub>C/C. Fig. S18 shows 3D-N-Ni<sub>3</sub>C/C also exhibited lower overpotential (103 mV) in 1.0 M KOH for HER compared to that of 3D-Ni<sub>3</sub>C/C (126 mV). Furthermore, in addition to the metal carbide system we designed, we have also seen similar effects of tungsten carbide and iron carbide in the reported papers [9,46,47]. The above results demonstrate that our strategy is possible to be extended to other N doped 3D electrocatalysts with enhanced catalytic property in HER.

### 3. Conclusions

In this work, it is the first time to uncover the fact that the high catalytic property of Mo<sub>2</sub>C in HER relies on the high nitrogen content on its surface by DFT-calculation. The calculation results indicate that the N doping can weaken the hydrogen adsorption ability by modifying the d- or p-band center of the atoms in the top layer, and thereby enhance the HER performance. Higher Mo-N content on the surface of Mo<sub>2</sub>C will bring more active sites for HER which is consistent with our experimental results. Guided by our DFT results, we develop a novel strategy to synthesize electrocatalysts for HER which can reduce the hydrogen absorption  $\Delta G_{\text{H}^*}$  and induce enhanced catalytic property. Based on this strategy, the effect of 3D-N-Mo<sub>2</sub>C/C with different Mo-N content was first calculated by our DFT simulation and later confirmed by our experiment. As expected, the sample with saturated N atoms on the surface of Mo<sub>2</sub>C exhibits excellent electrocatalytic performance in HER with low onset potential of 17 mV, low overpotential of 57 mV to reach the current density of 10 mA cm<sup>-2</sup>, small Tafel slope of 80 mV dec<sup>-1</sup>, robust stability and almost 100% Faradic efficiency in alkaline conditions. Moreover, this work highlights the potential of our nitrogen-doping strategy to design electrocatalysts with high performance for HER by extending to other metal carbide such as nickel carbide.

### Acknowledgments

This work was financially supported by National Natural Science Foundation of China (51772135, 21703081 and 21706090), Ministry of Education of China (6141A02022516), Natural Science Foundation of Guangdong Province (2014A030306010), Jinan University (88017418) and the Fundamental Research Foundation for the Central Universities (21617330, 21617326). We thank Ms. Biying Huang for her English editing service. We gratefully acknowledge the computational support by High-performance Super Computing Platform of Jinan University.

### Appendix A. Supplementary data

Supplementary material related to this article can be found, in the online version, at doi:<https://doi.org/10.1016/j.apcatb.2019.117891>.

### References

- [1] X. Long, G. Li, Z. Wang, H. Zhu, T. Zhang, S. Xiao, W. Guo, S. Yang, Metallic iron-nickel sulfide ultrathin nanosheets as a highly active electrocatalyst for hydrogen evolution reaction in acidic media, *J. Am. Chem. Soc.* 137 (2015) 11900–11903.
- [2] M.S. Balogun, W. Qiu, Y. Huang, H. Yang, R. Xu, W. Zhao, G.R. Li, H. Ji, Y. Tong, Cost-effective alkaline water electrolysis based on nitrogen-and phosphorus-doped self-supportive electrocatalysts, *Adv. Mater.* 29 (2017) 1702095.
- [3] B.R. Wygant, K. Kawashima, C.B. Mullins, Catalyst or precatalyst? The effect of oxidation on transition metal carbide, pnictide, and chalcogenide oxygen evolution catalysts, *ACS Energy Lett.* 3 (2018) 2956–2966.
- [4] X.P. Yin, H.J. Wang, S.F. Tang, X.L. Lu, M. Shu, R. Si, T.B. Lu, Engineering the coordination environment of single-atom platinum anchored on graphdiyne for optimizing electrocatalytic hydrogen evolution, *Angew. Chem. Int. Ed.* 57 (2018) 9382–9386.
- [5] G. Yang, S.A. Akhade, X. Chen, Y. Liu, M.S. Lee, V.A. Glezakou, R. Rousseau, J.A. Lercher, The nature of hydrogen adsorption on platinum in the aqueous phase, *Angew. Chem. Int. Ed.* 58 (2019) 3527–3532.
- [6] S. Li, C. Cheng, A. Sagaltchik, P. Pachfule, C. Zhao, A. Thomas, Metal-organic precursor-derived mesoporous carbon spheres with homogeneously distributed molybdenum carbide/nitride nanoparticles for efficient hydrogen evolution in alkaline media, *Adv. Funct. Mater.* 29 (2019) 1807419.
- [7] Y.T. Xu, X. Xiao, Z.M. Ye, S. Zhao, R. Shen, C.T. He, J.P. Zhang, Y. Li, X.M. Chen, Cage-confinement pyrolysis route to ultrasmall tungsten carbide nanoparticles for efficient electrocatalytic hydrogen evolution, *J. Am. Chem. Soc.* 139 (2017) 5285–5288.
- [8] H.B. Wu, B.Y. Xia, L. Yu, X.-Y. Yu, X.W.D. Lou, Porous molybdenum carbide nanooctahedrons synthesized via confined carburization in metal-organic frameworks for efficient hydrogen production, *Nat. Commun.* 6 (2015) 6512.
- [9] N. Han, K.R. Yang, Z. Lu, Y. Li, W. Xu, T. Gao, Z. Cai, Y. Zhang, V.S. Batista, W. Liu, Nitrogen-doped tungsten carbide nanoarray as an efficient bifunctional electrocatalyst for water splitting in acid, *Nat. Commun.* 9 (2018) 924.
- [10] G. Humagain, K. MacDougal, J. MacInnis, J.M. Lowe, R.H. Coridan, S. MacQuarrie, M. Dasog, Highly efficient, biochar-derived molybdenum carbide hydrogen evolution electrocatalyst, *Adv. Energy Mater.* 8 (2018) 1801461.
- [11] Y. Zhang, X. Xia, X. Cao, B. Zhang, N.H. Tiep, H. He, S. Chen, Y. Huang, H.J. Fan, Ultrafine metal nanoparticles/n-doped porous carbon hybrids coated on carbon fibers as flexible and binder-free water splitting catalysts, *Adv. Energy Mater.* 7 (2017) 1700220.
- [12] H. Jin, J. Chen, S. Mao, Y. Wang, Transition metal induced the contraction of tungsten carbide lattice as superior hydrogen evolution reaction catalyst, *ACS Appl. Mater. Interfaces* 10 (2018) 22094–22101.
- [13] J. Greeley, T.F. Jarillo, J. Bonde, I.B. Chorkendorff, J.K. Norskov, Computational high-throughput screening of electrocatalytic materials for hydrogen evolution, *Nat. Mater.* 5 (2006) 909–913.
- [14] G. Fu, X. Xu, P. Sautet, Inside cover: vanadium distribution in four-component Mo-V-Te-Nb mixed-oxide catalysts from first principles: how to explore the numerous configurations? *Angew. Chem. Int. Ed.* 51 (2012) 12630.
- [15] Y. Huang, J. Ge, J. Hu, J. Zhang, J. Hao, Y. Wei, Nitrogen-doped porous molybdenum carbide and phosphide hybrids on a carbon matrix as highly effective electrocatalysts for the hydrogen evolution reaction, *Adv. Energy Mater.* 8 (2018) 1701601.
- [16] Z. Shi, K. Nie, Z.-J. Shao, B. Gao, H. Lin, H. Zhang, B. Liu, Y. Wang, Y. Zhang, X. Sun, Phosphorus-Mo<sub>2</sub>C@ carbon nanowires toward efficient electrochemical hydrogen evolution: composition, structural and electronic regulation, *Energy Environ. Sci.* 10 (2017) 1262–1271.
- [17] Y. Zhang, B. Ouyang, J. Xu, G. Jia, S. Chen, R.S. Rawat, H.J. Fan, Rapid synthesis of cobalt nitride nanowires: highly efficient and low-cost catalysts for oxygen evolution, *Angew. Chem. Int. Ed.* 55 (2016) 8670–8674.
- [18] Q. Gao, W. Zhang, Z. Shi, L. Yang, Y. Tang, Structural design and electronic modulation of transition-metal-carbide electrocatalysts toward efficient hydrogen evolution, *Adv. Mater.* 30 (2018) 1802880.
- [19] Q. Mo, W. Zhang, L. He, X. Yu, Q. Gao, Bimetallic Ni<sub>2-x</sub>Co<sub>x</sub>P/N-doped carbon nanofibers: solid-solution-alloy engineering toward efficient hydrogen evolution, *Appl. Catal. B: Environ.* 244 (2018) 620–627.
- [20] Y. Huang, Q. Gong, X. Song, K. Feng, K. Nie, F. Zhao, Y. Wang, M. Zeng, J. Zhong, Y. Li, Mo<sub>2</sub>C nanoparticles dispersed on hierarchical carbon microflowers for efficient electrocatalytic hydrogen evolution, *ACS Nano* 10 (2016) 11337–11343.
- [21] L. Zhang, H. Yang, D.K. Wanigaratna, B. Liu, Ultrasmall transition metal carbide nanoparticles encapsulated in N, S-doped graphene for all-pH hydrogen evolution, *Small Methods* 2 (2018) 1700353.
- [22] J. Jia, T. Xiong, L. Zhao, F. Wang, H. Liu, R. Hu, J. Zhou, W. Zhou, S. Chen, Ultrathin N-doped Mo<sub>2</sub>C nanosheets with exposed active sites as efficient electrocatalyst for hydrogen evolution reactions, *ACS Nano* 11 (2017) 12509–12518.
- [23] J.R. Kitchin, J.K. Nørskov, M.A. Bartaeu, J. Chen, Role of strain and ligand effects in the modification of the electronic and chemical properties of bimetallic surfaces, *Phys. Rev. Lett.* 93 (2004) 156801.
- [24] J. Kitchin, J.K. Nørskov, M. Bartaeu, J. Chen, Modification of the surface electronic and chemical properties of Pt (111) by subsurface 3d transition metals, *J. Chem. Phys.* 120 (2004) 10240–10246.
- [25] M. Mavrikakis, B. Hammer, J.K. Nørskov, Effect of strain on the reactivity of metal surfaces, *Phys. Rev. Lett.* 81 (1998) 2819.
- [26] J. Lai, S. Li, F. Wu, M. Saqib, R. Luque, G. Xu, Unprecedented metal-free 3D porous carbonaceous electrodes for full water splitting, *Energy Environ. Sci.* 9 (2016) 1210–1214.
- [27] Z. Li, M. Shao, L. Zhou, Q. Yang, C. Zhang, M. Wei, D.G. Evans, X. Duan, Carbon-based electrocatalyst derived from bimetallic metal-organic framework arrays for high performance oxygen reduction, *Nano Energy* 25 (2016) 100–109.
- [28] M. Zhang, Q. Dai, H. Zheng, M. Chen, L. Dai, Novel MOF-derived Co@ N-C bi-functional catalysts for highly efficient Zn-air batteries and water splitting, *Adv. Mater.* 30 (2018) 1705431.
- [29] J. Wan, J. Wu, X. Gao, T. Li, Z. Hu, H. Yu, L. Huang, Structure confined porous Mo<sub>2</sub>C for efficient hydrogen evolution, *Adv. Funct. Mater.* 27 (2017) 1703933.
- [30] J. Jia, W. Zhou, Z. Wei, T. Xiong, G. Li, L. Zhao, X. Zhang, H. Liu, J. Zhou, S. Chen, Molybdenum carbide on hierarchical porous carbon synthesized from Cu-MoO<sub>2</sub> as efficient electrocatalysts for electrochemical hydrogen generation, *Nano Energy* 41 (2017) 749–757.
- [31] H. Wei, Q. Xi, X.a. Chen, D. Guo, F. Ding, Z. Yang, S. Wang, J. Li, S. Huang, Molybdenum carbide nanoparticles coated into the graphene wrapping N-doped

- porous carbon microspheres for highly efficient electrocatalytic hydrogen evolution both in acidic and alkaline media, *Adv. Sci.* 5 (2018) 1700733.
- [32] J. Gao, Z. Cheng, C. Shao, Y. Zhao, Z. Zhang, L. Qu, A 2D free-standing film-inspired electrocatalyst for highly efficient hydrogen production, *J. Mater. Chem. A* 5 (2017) 12027–12033.
- [33] Y.-Y. Chen, Y. Zhang, W.-J. Jiang, X. Zhang, Z. Dai, L.-J. Wan, J.-S. Hu, N. Pomegranate-Like, P-doped Mo<sub>2</sub>C@ C nanospheres as highly active electrocatalysts for alkaline hydrogen evolution, *ACS Nano* 10 (2016) 8851–8860.
- [34] Y. Zhao, K. Kamiya, K. Hashimoto, S. Nakanishi, In situ CO<sub>2</sub>-emission assisted synthesis of molybdenum carbonitride nanomaterial as hydrogen evolution electrocatalyst, *J. Am. Chem. Soc.* 137 (2014) 110–113.
- [35] Y.J. Tang, M.R. Gao, C.H. Liu, S.L. Li, H.L. Jiang, Y.Q. Lan, M. Han, S.H. Yu, Porous molybdenum-based hybrid catalysts for highly efficient hydrogen evolution, *Angew. Chem. Int. Ed.* 54 (2015) 12928–12932.
- [36] S. Jing, L. Zhang, L. Luo, J. Lu, S. Yin, P.K. Shen, P. Tsakaros, N-Doped porous molybdenum carbide nanobelts as efficient catalysts for hydrogen evolution reaction, *Appl. Catal. B: Environ.* 224 (2018) 533–540.
- [37] L. Lai, J.R. Potts, D. Zhan, L. Wang, C.K. Poh, C. Tang, H. Gong, Z. Shen, J. Lin, R.S. Ruoff, Exploration of the active center structure of nitrogen-doped graphene-based catalysts for oxygen reduction reaction, *Energy Environ. Sci.* 5 (2012) 7936–7942.
- [38] Y. Li, H. Li, K. Cao, T. Jin, X. Wang, H. Sun, J. Ning, Y. Wang, L. Jiao, Electrospun three dimensional Co/CoP@ nitrogen-doped carbon nanofibers network for efficient hydrogen evolution, *Energy Storage Mater.* 12 (2018) 44–53.
- [39] H.B. Yang, J. Miao, S.-F. Hung, J. Chen, H.B. Tao, X. Wang, L. Zhang, R. Chen, J. Gao, H.M. Chen, Identification of catalytic sites for oxygen reduction and oxygen evolution in N-doped graphene materials: development of highly efficient metal-free bifunctional electrocatalyst, *Sci. Adv.* 2 (2016) e1501122.
- [40] J.Y. Cheon, J.H. Kim, J.H. Kim, K.C. Goddeti, J.Y. Park, S.H. Joo, Intrinsic relationship between enhanced oxygen reduction reaction activity and nanoscale work function of doped carbons, *J. Am. Chem. Soc.* 136 (2014) 8875–8878.
- [41] F.X. Ma, H.B. Wu, B.Y. Xia, C.Y. Xu, X.W. Lou, Hierarchical β-Mo<sub>2</sub>C nanotubes organized by ultrathin nanosheets as a highly efficient electrocatalyst for hydrogen production, *Angew. Chem. Int. Ed.* 127 (2015) 15615–15619.
- [42] H. Lin, Z. Shi, S. He, X. Yu, S. Wang, Q. Gao, Y. Tang, Heteronanowires of MoC–Mo<sub>2</sub>C as efficient electrocatalysts for hydrogen evolution reaction, *Chem. Sci.* 7 (2016) 3399–3405.
- [43] K. Fan, H. Chen, Y. Ji, H. Huang, P.M. Claesson, Q. Daniel, B. Philippe, H. Rensmo, F. Li, Y. Luo, Nickel–vanadium monolayer double hydroxide for efficient electrochemical water oxidation, *Nat. Commun.* 7 (2016) 11981.
- [44] V. Vij, S. Sultan, A.M. Harzandi, A. Meena, J.N. Tiwari, W.-G. Lee, T. Yoon, K.S. Kim, Nickel-based electrocatalysts for energy-related applications: oxygen reduction, oxygen evolution, and hydrogen evolution reactions, *ACS Catal.* 7 (2017) 7196–7225.
- [45] H. Luo, H. Lei, Y. Yuan, Y. Liang, Y. Qiu, Z. Zhu, Z. Wang, Engineering ternary copper–cobalt sulfide nanosheets as high-performance electrocatalysts toward oxygen evolution reaction, *Catalysts* 9 (2019) 459.
- [46] S. Bukola, B. Merzougui, A. Akinpelu, M. Zeama, Cobalt and nitrogen Co-doped tungsten carbide catalyst for oxygen reduction and hydrogen evolution reactions, *Electrochim. Acta* 190 (2016) 1113–1123.
- [47] H. Jiang, Y. Yao, Y. Zhu, Y. Liu, Y. Su, X. Yang, C. Li, Iron carbide nanoparticles encapsulated in mesoporous Fe-N-doped graphene-like carbon hybrids as efficient bifunctional oxygen electrocatalysts, *ACS Appl. Mater. Interfaces* 7 (2015) 21511–21520.